Title

Electron Microscopy Study of the Passivating Layer on Iron-Nickel Martensite

Authors

Chen, Sheree H

Morris, J W

Publication Date

1976-02-01

Submitted to Metallurgical Transactions

LBL-4911 Rev.
Preprint

ELECTRON MICROSCOPY STUDY OF THE PASSIVATING LAYER ON IRON-NICKEL MARTENSITE

Sheree H. Chen and J. W. Morris, Jr.

February 1976

Prepared for the U. S. Energy Research and
Development Administration under Contract W-7405-ENG-48

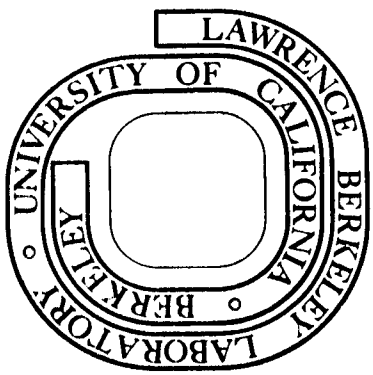

LBL-4911 Rev.

DISCLAIMER

ELECTRON MICROSCOPY STUDY OF THE PASSIVATING LAYER ON IRON-NICKEL MARTENSITE

by

Sheree H. Chen and J. W. Morris, Jr.

Department of Materials Science and Engineering and Materials and Molecular Research Division, Lawrence Berkeley Laboratory; University of California, Berkeley, California 94720

ABSTRACT

A passivating oxide layer is known to form rapidly on the surface of Fe or Fe alloys exposed to air at low temperature. The properties of this passivating layer largely control the low temperature oxidation and corrosion properties of iron. It is hence important that the nature of this passivating layer be well understood. The work reported here principally involved a transmission electron microscopy examination of the thin oxide film formed on the surface of Fe-12Ni alloys on exposure to air at room temperature. Using high resolution microscopy the oxide particles of the film could be directly resolved and their structure and morphology characterized. The following conclusions were drawn from these characterization studies: (1) A passivating oxide layer (principally Fe_3O_4) forms spontaneously on the surface of Fe-Ni alloys on exposure to air at room temperature. (2) The orientation relation between the oxide and the metal surface depends on surface orientation; the Bain relation is obeyed when the alloy surface is $(100)_\alpha$ while the Nishiyama-Wasserman relation is obeyed on other low index surfaces. This phenomenon is attributable to the need to

accommodate the misfit strain between the oxide and the substrate. (3) The oxide layer consists of dispersed, small ($\sim$20Å) oriented particles rather than a continuous thin film. (4) The size of the oxide particles and the density of their distribution is related to the crystal surface orientation and condition.

I. INTRODUCTION

The iron rich martensitic Fe-Ni base alloys (Ni concentration <29%) are important engineering materials due to their combination of high strength, high toughness and high corrosion resistance over a very wide temperature range.[1-5] The transmission electron microscopy study of the microstructure plays an essential role in the understanding of the origin of these promising properties. But the TEM study of Fe-Ni base alloys is often made difficult by the spontaneous formation of a thin oxide layer on the thin foil surface as soon as it is polished. The structure and the morphology of this thin oxide layer closely resembles those due to ordering or precipitation in the Fe-Ni martensite matrix. Thus oxide diffraction spots can easily be mistaken for superlattice diffraction spots of the matrix.[6,7] Moreover, high resolution dark field micrographs often exhibit a precipitate-like morphology which could reinforce the misinterpretation. Thus it is very necessary to clarify the existance and the structure of these thin oxide passivating layers.

The morphology and structure of these thin oxide layers on the Fe-Ni metal surface is also important in the understanding of oxide passivation and corrosion resistance. At high temperature, the oxidation rate is very fast, following the parabolic approximation, and the initial transient stage is too short to be observed. However, the slow oxidation rate of Fe-Ni alloys at room temperature allows the study of the initial stages of oxidation. The low temperature oxidation behavior is shown schematically in Figure 1, based on previous experimental data.[8,9] Initially, the oxidation rate is linear and can be

approximated by the dotted line AM. During this period, the oxygen gas is spontaneously adsorbed on the metal surface[9-11] and forms nuclei by the place exchange mechanism.[9,10,12-14] Later the growth of the thin oxide layer follows the logarimatic rate approximation, approaching a limiting thickness (BC) and finally a steady state (CD).[13,15-18] The properties of this steady state oxide layer control corrosion behavior by controlling the time at which breakaway occurs (DE).[19,20] After breakaway occurs the oxidation rate is extremely fast and follows a linear rate law.[19]

Several low temperature oxidation studies on Fe and Fe-Ni alloys have been published,[7,21-25] but the conclusions are conflicting. Gillet et al.[21] and Wagner et al.[22] suggested that the oxide phase is Fe_3O_4 with the usual spinal structure and that the orientation relationship between the Fe_3O_4 and the b.c.c. α substrate is of the Bain type (Fig. 2).[26] Keown et al.[24] agreed with the Fe_3O_4 structure but disagreed with the Bain relationship and suggested instead the Nishiyama[27] and Wasserman[28] relationship (Fig. 3). In addition, they proposed a multi-zone model to explain the appearance of forbidden diffractions in the $[100]_\alpha$ zone orientation. A reconsideration of these proposed structures, models and explanations is one of the purposes of this paper.

The morphology of this oxide passivating layer can be observed using the high resolution dark field image technique. This technique allows not only an observation of the layer, but also a study of the actual behavior of the low temperature oxidation process in Fe-Ni alloys. This is the other purpose of this investigation.

II. EXPERIMENTAL PROCEDURE

The primary material investigated here was an Fe-12Ni binary alloy. The investigation was extended to Fe-12Ni-0.25Ti, Fe-6Ni-2Mn, Fe-8Ni-4Mn and Fe-25Ni alloys, which are under investigation in this laboratory because of their cryogenic properties.[2,29] The chemical compositions are given in Table I. All the materials yielded similar experimental results.

The ingots were homogenized under vacuum at 1473°K for 48 hours, furnace cooled, cross forged into 2 cm thick plates at ∿1373°K and then air cooled to room temperature. The plates were then cut into 3×2×2 cm^3 blocks. The heat treatments are given in Table II. Thin slices of 3×2×0.05 cm^3 size were taken from the interior of these blocks to prepare thin foils. One of these thin sliced specimens was then selected for heat treatment at 1273°K for five hours in a hydrogen furnace.

The slices were chemically polished to 0.0025∿0.005 cm thickness in an electrolyte containing 20 ml H_2O_2 and 15 drops HF. The polished specimens were then cut into discs with a spark machine and subjected to five different kinds of polishing techniques (Table III).

The transmission electron microscopy was carried out on a Philips 301 electron microscope equipped with a high tilting stage, a high resolution stage and a hot stage. The operating voltage was 100 kV.

III. RESULTS

It was found that diffraction patterns taken from the freshly polished clean samples do show diffraction spots other than those of the Fe-Ni solid solution α-phase (Fig. 4-Fig. 7). In order to eliminate the possibility that these additional diffractions were due to ordered phases, precipitate phases or internal oxide particles, a series of heat treatments was done. This series included a very fast quenching treatment from extremely high temperature, an extended aging treatment done after vacancy saturation, and high temperature hydrogen furnace annealing. It was found that the additional phase is heat treatment independent. Thus, it was tentatively concluded that the phase was not internal to the Fe-Ni martensite matrix.

In order to determine whether the superlattice spots are due to an artifact of the polishing process, the specimens were subjected to various kinds of thinning procedures. These included both different polishing solutions and different polishing techniques, for instance, jet polish, window polish and an ion thinning procedure which was preceeded by jet polishing. The extra spots persisted, independent of polishing technique. Given the conclusion of previous researchers[5,8-20] that the formation of the passivating layer on the sample surface is unavoidable, it was hence reasonable to conclude that this peculiar structure corresponding to the passivating surface layer formed either during or immediately after the sample was polished.

A. Electron Diffraction Analysis

Four different orientations of selected area electron diffraction patterns were taken from freshly polished samples, and are shown in Figure 4 through Figure 8 together with their analysis. As described below, it may be concluded from this evidence that:

(1) each diffraction pattern contains one variant of body-centered cubic (b.c.c.) α-iron nickel solid solution phase and another one or two variants of a cubic spinel structure phase, (2) the face-centered cubic (f.c.c.) spinel structure is due to the oxide phase of Fe_3O_4 or $NiFe_2O_4$, (3) the orientation relationship between the α-iron nickel solution phase and the oxide phase follows either the well-known Bain relationship[26] as illustrated in Figure 2[30] or the Nishiyama[27] and Wasserman[28] (N-W) relationship as shown in Figure 3,[30] depending on the foil orientation.

The lattice parameters of the crystal structures were calibrated using a standard gold ring pattern. The lattice parameter of b.c.c. α-iron nickel solid solution phase was determined to be 2.87 ± 0.05Å, consistent with previous X-ray experimental data. The lattice parameter of the spinel phase was calibrated as 8.36 ± 0.05Å. This value is common to the Fe_3O_4 and $NiFe_2O_4$ oxide spinel structures according to standard X-ray data. However, of the various oxides of iron, Fe_3O_4 is thermodynamically preferred under the condition of formation of the passivating layer. The lattice parameter of Fe_3O_4, 8.3963Å, and that of $NiFe_2O_4$, 8.339Å, are too close to determine whether this oxide spinel phase is Fe_3O_4 or $NiFe_2O_4$ from the electron diffraction data.

The diffraction pattern in Fig. 4(a) was taken from an area with $[100]_{\alpha}$ and also $[\underline{100}]_{oxide}$ zone orientation. From the analysis shown in Fig. 4(b),

$$[\underline{100}]_{oxide} \;||\; [100]_{\alpha}$$
$$(\underline{010})_{oxide} \;||\; (01\bar{1})_{\alpha}$$
$$(\underline{001})_{oxide} \;||\; (011)_{\alpha}$$

The orientation relationship between the α and the oxide phase follows the Bain relationship, Fig. 2. Only one variant of the oxide phase is present. This result is consistant with that of Wagner et al.,[22] but disagrees with the conclusion of Keown et al.[24] The consequence of this result will be discussed later.

The diffraction pattern in Fig. 5(a) was taken with crystal orientation close to the $[\bar{1}10]_{\alpha}$ or $[110]_{\alpha}$ zone. These two matrix orientations give identical diffraction patterns and surface structures, by symmetry. In Fig. 5(b) the matrix diffraction pattern is indexed assuming the $[110]_{\alpha}$ orientation. Indices corresponding to the $[\bar{1}10]_{\alpha}$ orientation are also shown (in brackets). Two oxide zones, $[\underline{\bar{1}11}]_{oxide}$ and $[\underline{211}]_{oxide}$ are present together in this diffraction pattern. The orientation relations are

$$(\underline{0\bar{1}1})_{oxide} \;||\; (001)_{\alpha}$$
$$(\underline{\bar{1}11})_{oxide} \;||\; (\bar{1}10)_{\alpha}$$

and the angle between $(\underline{101})_{oxide}$ and $(111)_{\alpha}$ is about 5°, $(\underline{110})_{oxide}$ and $(11\bar{2})_{\alpha}$ about 23° and $(\underline{1\bar{3}1})_{oxide}$ and $(1\bar{1}2)_{\alpha}$ about 4°. All of these are consistant with the N-W relationship shown in Fig. 3. Fig. 3 also shows

the orientation relationships $[\underline{\bar{1}11}]_{oxide} \parallel [\bar{1}10]_{\alpha}$ and $[\underline{211}]_{oxide} \parallel [110]_{\alpha}$. Since these two matrix orientations are identical by symmetry, both oxide variants are expected to appear on the surface.

The diffraction patterns, Figs. 6(a) through 6(d), show the crystal in the $[\bar{2}10]_{\alpha}$ or $[120]_{\alpha}$ orientation. These orientations are also identical by symmetry. The index of the matrix diffraction pattern is given for the $[120]_{\alpha}$ orientation, with the corresponding $[\bar{2}10]_{\alpha}$ indices shown in brackets. Again, two oxide variants appear, of which one is in the $[\underline{\bar{2}11}]_{oxide}$ zone orientation and the other in the $[\underline{111}]_{oxide}$ zone. The angles between the oxide diffractions and the b.c.c. α-phase diffractions exactly follow those of the N-W relationship. Also, according to Fig. 3, the angles between the $[\bar{2}10]_{\alpha}$ and $[\underline{\bar{2}11}]_{oxide}$, and the $[120]_{\alpha}$ and $[\underline{111}]_{oxide}$ direction are both $\sim 1°$ in the N-W relationship. Therefore the N-W relationship also explains why the $[\underline{\bar{2}11}]_{oxide}$ and $[\underline{111}]_{oxide}$ orientations occur simultaneously on the $\{210\}_{\alpha}$ surface. In Fig. 7(a) through (d), the sample orientation is located between the $[3\bar{1}1]_{\alpha}$ and $[2\bar{1}1]_{\alpha}$ zones, but is closer to the $[2\bar{1}1]_{\alpha}$ zone. As expected from Fig. 3, the $[\underline{1\bar{1}0}]_{oxide}$ zone appears in Fig. 7(a). Diffraction patterns were also studied for a number of additional orientations of the iron foil, including the $[111]_{\alpha}$, $[113]_{\alpha}$, $[130]_{\alpha}$ and $[122]_{\alpha}$ zones. The results were as given above; the N-W relation is obeyed. The present investigation hence shows that the orientation relationship follows the Bain relationship when the crystal surface is in the $[100]_{\alpha}$ orientation, and the N-W relationship when it is in other low index surface orientations.

The occurrence of the forbidden diffraction spots $\{\underline{113}\}_{oxide}$ and $\{\underline{115}\}_{oxide}$ in the diffraction patterns near the $[100]_{\alpha}$ and $[\underline{100}]_{oxide}$

orientation (Fig. 8) causes some ambiguity in the interpretation of the electron diffraction pattern. These anomalies can, however, be attributed to relrod effects due to the small size of the diffracting particles. According to Thomas et al.[31] and Hirsh et al.,[32] in the very thin regions of the foil (e.g. near the edge) where the relrods of the reciprocal lattice points are quite long, it is possible that the relrods from the next layer of reciprocal lattice intersect the reflecting sphere and give rise to forbidden reflections. The unit vector of reciprocal lattice of Fe_3O_4 or $Ni_xFe_{3-x}O_4$ is $1/8.36\mathring{A} \approx 0.12\mathring{A}^{-1}$. The half-width of the central peak of an oxide diffraction can be calculated as 1/w; w is the thickness of the thin oxide layer. If we assume w = $20\mathring{A}$,[4,5,9] then $1/w \approx 0.05\mathring{A}^{-1}$ which is almost one half of the reciprocal lattice vector. The existence of satellites about the central peak will make the peak appear still larger, as illustrated in Fig. 9. Therefore, it is not surprising that some bending of the specimen or a small deviation from the exact symmetrical orientation will result in the occurrence of the forbidden first Laue zone diffraction spots. Comparing the angle between the $\bar{g}$ vectors shown on the diffraction path by Fig. 8[9] with the angle calculated from the equation

$$\cos\theta = \frac{h_1h_2 + k_1k_2 + \ell_1\ell_2}{\sqrt{h_1^2 + k_1^2 + \ell_1^2}\ \sqrt{h_2^2 + k_2^2 + \ell_2^2}}$$

the diffraction pattern can be indexed as shown in Fig. 8(c). Since $hu + kv + \ell w = 1$ for $(\underline{113})_{oxide}$, $(\underline{115})_{oxide}$, $(\underline{1\bar{1}3})_{oxide}$, and $(\underline{1\bar{1}5})_{oxide}$ while $Hu + kv + \ell w = -1$ for $(\underline{\bar{1}\bar{1}\bar{3}})_{oxide}$, $(\underline{\bar{1}\bar{1}\bar{5}})_{oxide}$, $(\underline{\bar{1}1\bar{3}})_{oxide}$, and $(\underline{\bar{1}1\bar{5}})_{oxide}$, all diffraction spots are accounted for if it is assumed

that the foil orientation deviates slightly from $[100]_\alpha$; hence the Ewald sphere is tilted slightly with respect to the exact $[\underline{100}]_{oxide}$ zone axis (Fig. 9). The disappearance of the forbidden spots in the exact $[100]_\alpha$ orientation (Fig. 4) supports this interpretation.

Since the thinnest area of the foil (i.e. near the edge) was examined in the present investigation for the purpose of obtaining very high resolution dark field images, forbidden diffraction spots occur not only from oxide phase but also from b.c.c. α-phase. In Fig. 6(a) the two additional spots indicated as triangles are due to the next layer of the reciprocal lattice and are $(110)_\alpha$ and $(\bar{1}\bar{1}0)_\alpha$ diffractions which are forbidden in $[\bar{2}10]_\alpha$ zone. In Fig. 7 the angle between the $[3\bar{1}1]_\alpha$ zone and the $[2\bar{1}1]_\alpha$ zone is 10.03°. These two zones occur simultaneously, probably because of the streaking of the diffraction spots.

B. The Morphology of the Thin Oxide Layer

By using high resolution dark field electron microscopy, it was found that the oxide layer formed at room temperature consists of extremely fine oxide particles as shown in Fig. 10. This morphology can be explained in terms of a relatively large number of nucleation sites at the surface of the foil with a rather limited growth rate at room temperature.

Figure 10(a) is a dark field image from the $(\underline{113})_{oxide}$ diffraction when the foil is in the $[113]_\alpha$ orientation. A dark field taken from a $(\underline{404})_{oxide}$ spot from a region with $[110]_\alpha$, $[\underline{111}]_{oxide}$ and $[\underline{112}]_{oxide}$ zone axes is shown in Fig. 10(b) and indicates that the particles are 10∿30Å size, of irregular shape, and lower density than the other two

orientations shown. Fig. 10(c) shows a dark field micrograph from the $(\underline{113})_{oxide}$ diffraction, illustrating the detailed morphology of the thin oxide layer with the sample approximately normal to the $[100]_{\alpha}$ and $[\underline{100}]_{oxide}$ direction.

The density of the oxide particles in the region with crystal surface close to the $[110]_{\alpha}$ orientation is apparently much less than that on crystal surfaces in the $[100]_{\alpha}$ and $[113]_{\alpha}$ orientations. Previous research indicates that the epitaxial growth rate of thin oxide layers is very much orientation dependent.[9,18] The most closely packed plane in α-iron is the $(110)_{\alpha}$ plane. Since the oxygen atom has less contact with the metal surface on the closest packed surface than on other orientations the formation of oxide on the surface with $[110]_{\alpha}$ orientation is expected to be relatively difficult. However, the surface of the thin transmission electron microscopy specimen is not exactly $[110]_{\alpha}$ oriented throughout, and the oxygen atoms will preferentially aggregate on ledges to form the nuclei. This is believed to be a principle cause for the wide separation of oxide particles on the $[110]_{\alpha}$ surface.

Careful examination of diffraction spots from the oxide phase reveals that the diffraction spots are elongated perpendicular to the radial direction, and that the higher the index the longer is the elongation. These observations indicate the existence of a slight misorientation of these tiny particles on the sample surface which is probably due to the roughness of the surface or thermal statistical rotations of the small islands on the substrate surface.

IV. DISCUSSION

1. Reason for Spontaneous Oxidation

Surface adsorption has been shown to occur spontaneously whenever a clean metal surface is brought into contact with a gas.[5,9,10] There are two possible mechanisms which could account for this adsorption: physical reactions and/or chemical reactions. The occurrence of chemisorption can be determined by the Rideal and Jones equation[17,18,33]

$$\Delta E = \phi - K$$

where ΔE is the activation energy, ϕ the work function which represents the energy required to move the electrons across the metal/gas interface. K is the sum of the electron affinity, the dissociation energy and the energy associated with adsorption for a given gas molecule.[34] When the work function ϕ is less than K, the activation energy ΔE will be negative, and no energy barrier will exist. For the chemical adsorption of oxygen molecules on the surface or iron, ΔE is approximately -5.65×10^5 J/mole.[4,9] Hence, it is reasonable to expect that the oxygen atoms will automatically be chemisorbed on the Fe-Ni TEM sample surface as soon as it is polished. For the physical adsorption of oxygen, the energy barrier is about 2.09×10^4 J/mole.[9] Thus it is reasonable to expect the physical or chemical reaction may proceed to some extent even at room temperature. The reason why an oxide layer forms first on the α-FeNi solid solution surface rather than a nitride layer or a hydride layer can be also explained by Rideal and Jones' equation. The ionization energy of N_2 and H_2 are 1.50×10^6 J/mole and 1.49×10^6 J/mole which are much larger than that of oxygen, 1.16×10^6 J/mole[35] so that the

constants K for N_2 and H_2 are smaller than that of oxygen. It is found that[36,37] the activation energy ΔE of forming nitride and hydride on the surface of iron in atmosphere is about $-1.25\times10^5 \sim -1.67\times10^5$ J/mole which is relatively less negative than that of oxide formation. Therefore, the oxygen molecules are first picked up by the metal to form an oxide. In addition to this, both the carbon dioxide gas and the water vapor which are in the atmosphere could contribute to the oxidation of α Fe-Ni alloys.

2. Nature of the Adsorbed Phase

It is known that the lattice parameters and the structures of Fe_3O_4 and $NiFe_2O_4$ are too similar to be distinguished from each other by electron diffraction analysis alone. However, the electrode potential for Fe (-0.44 eV) is higher than that of Ni (-0.25 eV),[35] and Ni is more stable than iron. It is expected that during the oxidation of Fe-Ni martensite, iron will be selectively oxidized first, leaving a nickel-enriched zone due to the depletion of iron atoms. When the Ni concentration inside the Ni-enriched zone reaches a certain level, the $Ni_xFe_{3-x}O_4$ phase starts to form, the value of x being a function of Ni concentration in the matrix, temperature and the distance to the metal oxide surface.[5,38] Therefore it is presumed that the spinel phase formed spontaneously at room temperature is either Fe_3O_4 or $Ni_xFe_{3-x}O_4$ with very small x value.

3. Orientation Relation

The reason why the grains with $[100]_\alpha$ orientation show the Bain relationship while the other orientations show the N-W relationship, can be explained from strain energy considerations. It is well known[39] that an f.c.c. structure with a lattice parameter close to $\sqrt{2}$ times that of a b.c.c. structure can be derived by rotating the b.c.c. lattice by 45° around the $\vec{c}$ axis, and then expanding the $\vec{c}$ axis of the b.c.c. lattice to match the lattice difference in the c direction. This is the origin of the Bain relationship. The lattice parameter of the Fe_3O_4 spinel structure is about 8.36Å or approximately $2\sqrt{2}$ times the lattice parameter of α-iron nickel, 2.87Å. When the f.c.c. phase

grows epitaxially on the α-iron nickel surface along the $(100)_\alpha$ orientation, the c-axis is perpendicular to the surface; hence its contribution to the strain energy is zero and the Bain relationship is followed. When the f.c.c. phase grows on a surface of α-iron nickel with orientation other than $(100)_\alpha$, the lattice mismatch along the $\vec{c}$ axis is prominent and the strain energy due to this has to be taken into consideration. Then the familiar N-W relationship is followed by 9° rotation from Bain relationship to minimize the strain energy.

In contrast to our conclusion that Fe_3O_4 is Bain related to α-Fe on the $(100)_\alpha$ surface, Keown et al.[24] concluded that the N-W relationship holds at all the orientations. However, to apply their interpretation to the oxide present on the $(100)_\alpha$ foil surface, one must assume the presence of at least three oxide variants whose orientation with the substrate is off by several degrees from the N-W prescription. No such complexity occurs when the Bain relation is assumed; all diffraction spots are then attributable to fundamental reflections or relrod effects from a single oxide variant as described above.

4. Oxide Morphology

The principal observation concerning oxide morphology is that the oxide film consists of small, discrete particles which do not completely cover the sample surface. This observation suggests that the particles form predominantly by heterogeneous nucleation at favorable sites which are saturated either by consumption or poisoning before a complete oxide film is established. The linear strings of particles commonly

observed in the dark field micrographs (Figure 10) suggest that the favorable sites are often ledges in the crystal surface. The observation that the particles often cease growth before impingement, and are hence seen as separate particles on the surface, may simply be due to the accumulation of elastic strain due to particle growth; even when favorably oriented the oxide particles retain a lattice mismatch of ∿2.9% with the substrate. Other mechanisms, such as impurity accumulation at the growing interface, may also play a role.

The discrete particle morphology of the oxide layer may contribute to the oxidation resistance of the alloy since the particles may form a protective coating without sustaining the high internal stress which would be present if the oxide formed as a continuous film. Such unrelaxed stresses would make the film liable to failure and promote cracking and consequent break away of the protective layer.[19,20,40,41]

V. CONCLUSIONS

(1) Passivating oxide layers form spontaneously on Fe-Ni alloys, independent of previous heat treatment. The passivating oxide layers have spinel structures and consist of Fe_3O_4 or $Ni_xFe_{3-x}O_4$ with low x value. (2) The orientation between the oxide passivating layer and the metal matrix follows the Bain relationship when the crystal surface is in the $(100)_\alpha$ orientation, and the Nishiyama and Wasserman relationship when the crystal surface is in other low index plane orientation. The forbidden diffraction spots appearing in the $[100]_\alpha$ and $[\underline{100}]_{oxide}$ zone orientation, are due to streaking from the next reciprocal lattice layer. (3) The oxide layers consist of dispersed tiny orientated

particles insteady of continuous thin films. (4) The size and the density of distribution of the oxide particles are related to the crystal surface orientation and condition.

ACKNOWLEDGMENTS

The authors wish to acknowledge helpful discussions with Professor G. Thomas. This research was supported by the Office of Naval Research under Contract NOOO14-75-C-0154 and by the U.S. Energy Research and Development Administration through the Materials and Molecular Research Division of the Lawrence Berkeley Laboratory.

REFERENCES

1. S. Floreen: Met. Rev., 1968, vol. 126, p. 115.

2. S. Jin, J. W. Morris, Jr. and V. F. Zackay: Met. Trans., 1975, vol. 6A, p. 141.

3. W. S. Owen, E. A. Wilson and T. Bell: *High Strength Materials*, V. F. Zackay, ed., p. 167, John Wiley and Sons, Inc., New York, 1965.

4. J. Kruger and H. T. Yolken: Corrosion, 1964, vol. 20, p. 29.

5. R. T. Foley: J. Electrochemical Society, 1962, vol. 109, p. 1202.

6. E. Tekin and P. M. Kelly: JISI, 1965, vol. 203, p. 715.

7. E. Smith: Acta Met., 1966, vol. 14, p. 583.

8. W. D. Tomashov: *Theory of Corrosion and Protection of Metals*, translated and edited by B. H. Tytell, I. Geld and H. S. Preser, p. 56, p. 81, The MacMillan Company Press, New York, 1966.

9. F. P. Fehlner and N. F. Mott: Oxidation of Metals, 1970, vol. 2, p. 59.

10. G. Ehlich: *1961 Trans. 8th Vacuum Symposium and 2nd International Cong.*, p. 126, Pergamon Press, New York, 1962.

11. R. Smoluchowski: Phys. Rev., 1941, vol. 60, p. 611.

12. M. A. H. Lanyon and B. M. W. Trapnell: Proc. Roy. Soc. A, 1955, vol. 227, p. 387.

13. M. Wyn Roberts: Quart. Rev. (London), 1962, vol. 16, p. 71.

14. D. D. Eley and P. R. Wilkinson: Proc. Roy. Soc. A, 1960, vol. 254, p. 327.

15. N. F. Mott: Trans. Faraday Soc., 1947, vol. 43, p. 429.

16. N. Cabrera and N. F. Mott: Rept. Progr. Phys., 1948-49, vol. 12, p. 163.

17. H. Uhlig: Acta Met., 1956, vol. 4, p. 541.

18. H. Uhlig, J. Pickett and J. MacNairn: Acta Met., 1959, vol. 7, p. 111.

19. A. U. Seybolt: Advan. Phys., 1963, vol. 12, p. 1.

20. D. A. Vermilyea: Acta Met., 1957, vol. 5, p. 492.

21. M. Gillet et al.: *Proc. of the 3rd Reg. Conf. on Electron Microscopy, Prague*, 1964, p. 379.

22. J. B. Wagner, Jr. et al.: Trans. AIME, 1961, vol. 221, p. 257.

23. I. A. Menzies and J. Lubkiewicz: Oxidation of Metals, 1971, vol. 3, p. 41.

24. S. R. Keown and D. J. Dyson: JISI, 1966, vol. 204, p. 832.

25. A. T. Davenport: JISI, 1968, vol. 206, p. 499.

26. E. C. Bain: Trans. AIME, 1924, vol. 60, p. 25.

27. Z. Nishiyama: Scien. Rep. Tohoku University, 1934, vol. 23, p. 638.

28. G. Wasserman: Arch. fur das Eisenhutt, 1933, vol. 16, p. 647.

29. S. Jin, S. K. Hwang and J. W. Morris, Jr.: Met. Trans. A, 1975, vol. 6A, p. 1721.

30. K. W. Andrews, D. J. Dyson and S. R. Keown: *Interpretation of Electron Diffraction Patterns*, pp. 146-147, Plenum Press, New York, 1967.

31. G. Thomas, W. L. Bell and H. M. Otte: Phys. Stat. Sol., 1965, vol. 12, p. 353.

32. P. B. Hirsch et al.: *Electron Microscopy of Thin Crystals*, Butterworth, London, 1965.

33. E. Rideal and O. Wansbrough Jones: Proc. Roy. Soc., 1929, vol. 123A, p. 202.

34. G. Ehlich: J. Chem. Phys., 1959, vol. 31, p. 1111.

35. *Handbook of Chemistry and Physics*, R. C. Weast, ed., 5th ed., CRC Press, 1973-74.

36. D. Brennan, D. O. Hayward and B. M. W. Trapnell: Proc. Roy. Soc., 1960, vol. A256, p. 81.

37. J. Bagg and F. C. Tompkins: Trans. Faraday Soc., 1955, vol. 51, p. 1071.

38. M. J. Brabers and C. E. Birchenall: Corrosion, 1958, vol. 14, p. 33.

39. M. S. Wechsler, D. S. Lieberman and T. A. Read: Trans. AIME, 1953, vol. 197, p. 1503.

40. B. Chattupadhyay and G. C. Wood: Oxidation of Metals, 1970, vol. 2, p. 373.

41. D. L. Douglass: Oxidation of Metals, 1969, vol. 1, p. 127.

Table I

Chemical Compositions (wt. %)

	Fe	Ni	Cr	Mn	C	N	S	P	Ti
Fe-12Ni-0.25Ti	Bal.	12.07	--	--	0.001	0.014	0.004	0.003	0.26
Fe-12Ni	Bal.	12.04	--	--	0.002	0.003	0.002	0.001	0.006
Fe-8Ni-2Mn	Bal.	8.03	--	1.97	0.001	0.001	0.006	0.001	0.17

Table II

Thermal Treatments

a-1	As annealed
a-2	a-1 + 573°K/30 min. in vacuum sealed quartz + ice brine quench
a-3	a-2 + 873°K/8 hrs. in dynamic argon gas
a-4	a-2 + 773°K/8 hrs. in dynamic argon gas
a-5	a-1 + 923°K/1 month in air
a-6	A-1 + 823°K/1 month in air
a-7	a-1 + 1173°K/8 hrs.

Table III

Polishing Techniques

c-1	Ordinary jet polishing technique using a solution containing 150 g Cr_2O_3, 800 ml CH_3COOH and 40 ml of water.
c-2	Ordinary jet polishing technique with solution containing 10% perchloric acid, 90% acetic acid.
c-3	Window technique with the solution similar to c-1.
c-4	Chemical polish with HF + H_2O_2.
c-5	c-1 plus ion thinner technique.

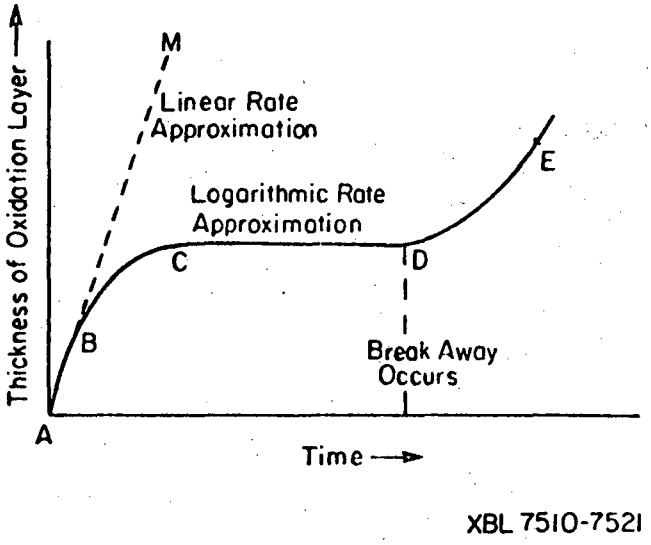

Fig. 1. Low temperature oxidation behavior.

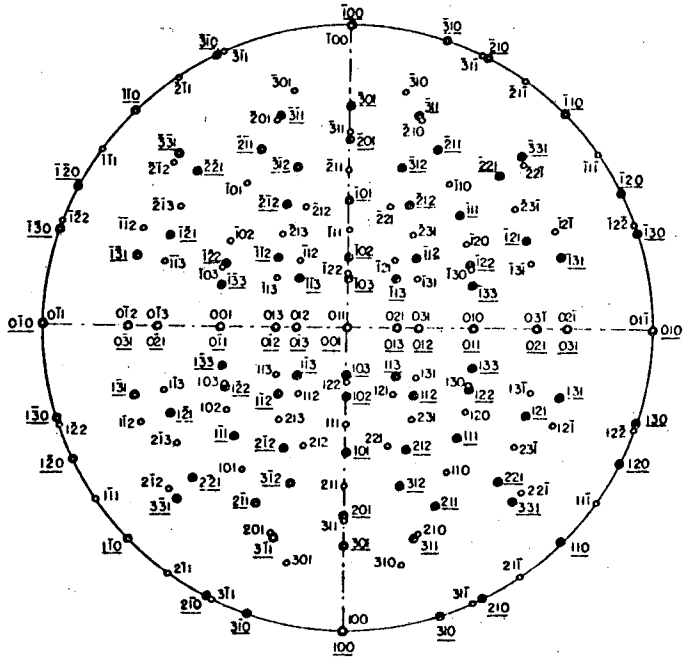

XBL 7510-7520A (a)

Fig. 2. Stereographic projection representing the Bain relationship between body- and face-centered cubic materials

$$(100)_{b.c.c.} \parallel (\underline{100})_{f.c.c.}$$

$$(01\bar{1})_{b.c.c.} \parallel (\underline{010})_{f.c.c.}$$

$$(011)_{b.c.c.} \parallel (\underline{001})_{f.c.c.}$$

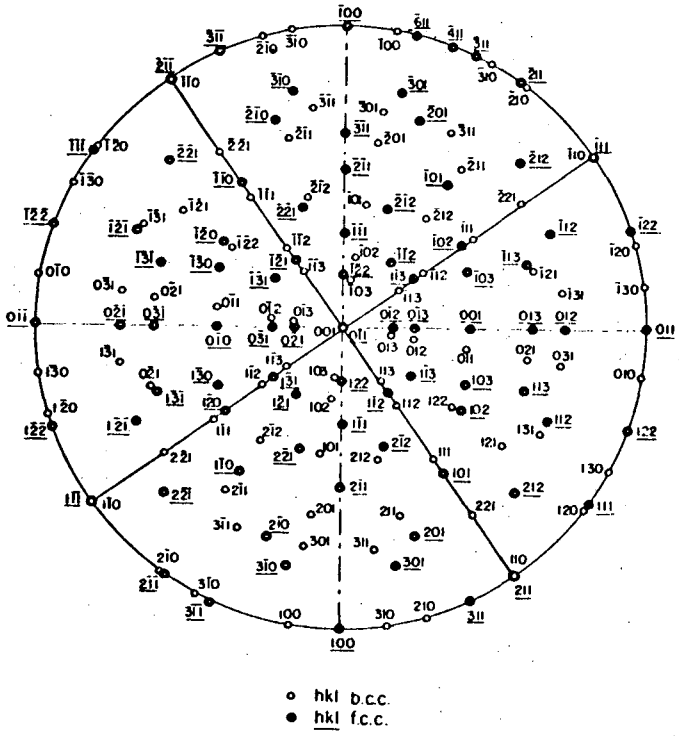

XBL 7510-7520A (b)

Fig. 3. Stereographic projection representing the Nishiyama and Wasserman (N-W) relationship between body- and face-centered cubic materials

$$(001)_{b.c.c.} \parallel (0\bar{1}1)_{f.c.c.}$$

$$(\bar{1}10)_{b.c.c.} \parallel (\bar{1}\underline{11})_{f.c.c.}$$

$$(110)_{b.c.c.} \parallel (\underline{211})_{f.c.c.}$$

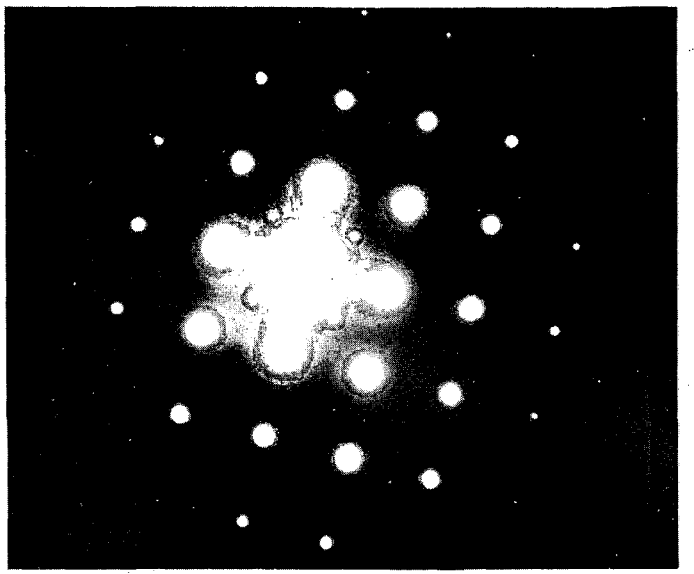

A

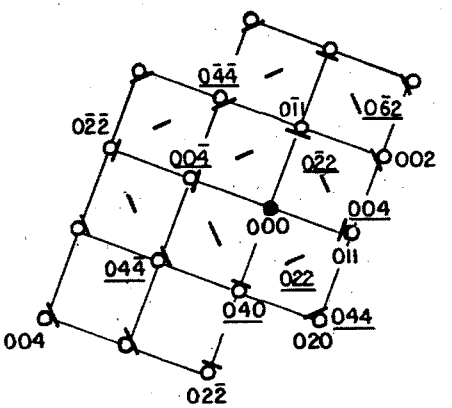

B

XBB 7512-9242

Fig. 4. (a) Diffraction pattern taken from an area showing the $[100]_{\alpha}$ zone and $[\underline{100}]_{oxide}$ zone.

(b) Index of the diffraction pattern (o - $[100]_{\alpha}$ zone; / - $[\underline{100}]_{oxide}$ zone).

A

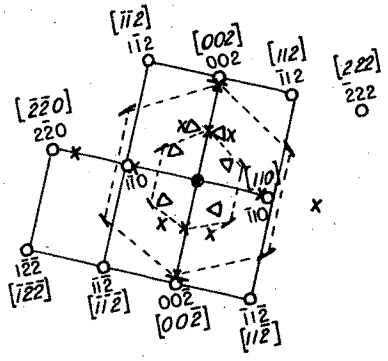

B

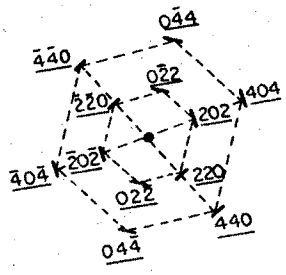

C

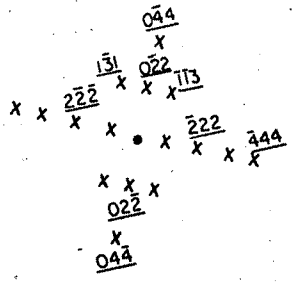

D XBB 7512-9240

Fig. 5. (a) Diffraction pattern taken from an area showing the $[110]_{\alpha}$ zone (or $[\bar{1}10]_{\alpha}$ zone) and two variants of the oxide ($[\underline{\bar{1}11}]_{oxide}$ and $[\underline{211}]_{oxide}$ zones). (b) Index of the diffraction pattern (o - [110] zone of $[\bar{1}10]_{\alpha}$ zone. x - $[\underline{211}]_{oxide}$ zone. / - $[\underline{\bar{1}11}]_{oxide}$ zone. Δ - Double diffraction spots). (c) Index of the $[\underline{\bar{1}11}]_{oxide}$ zone corresponding to the $[\bar{1}10]_{\alpha}$ zone. (d) Index of the $[\underline{211}]_{oxide}$ zone corresponding to the $[110]_{\alpha}$ zone.

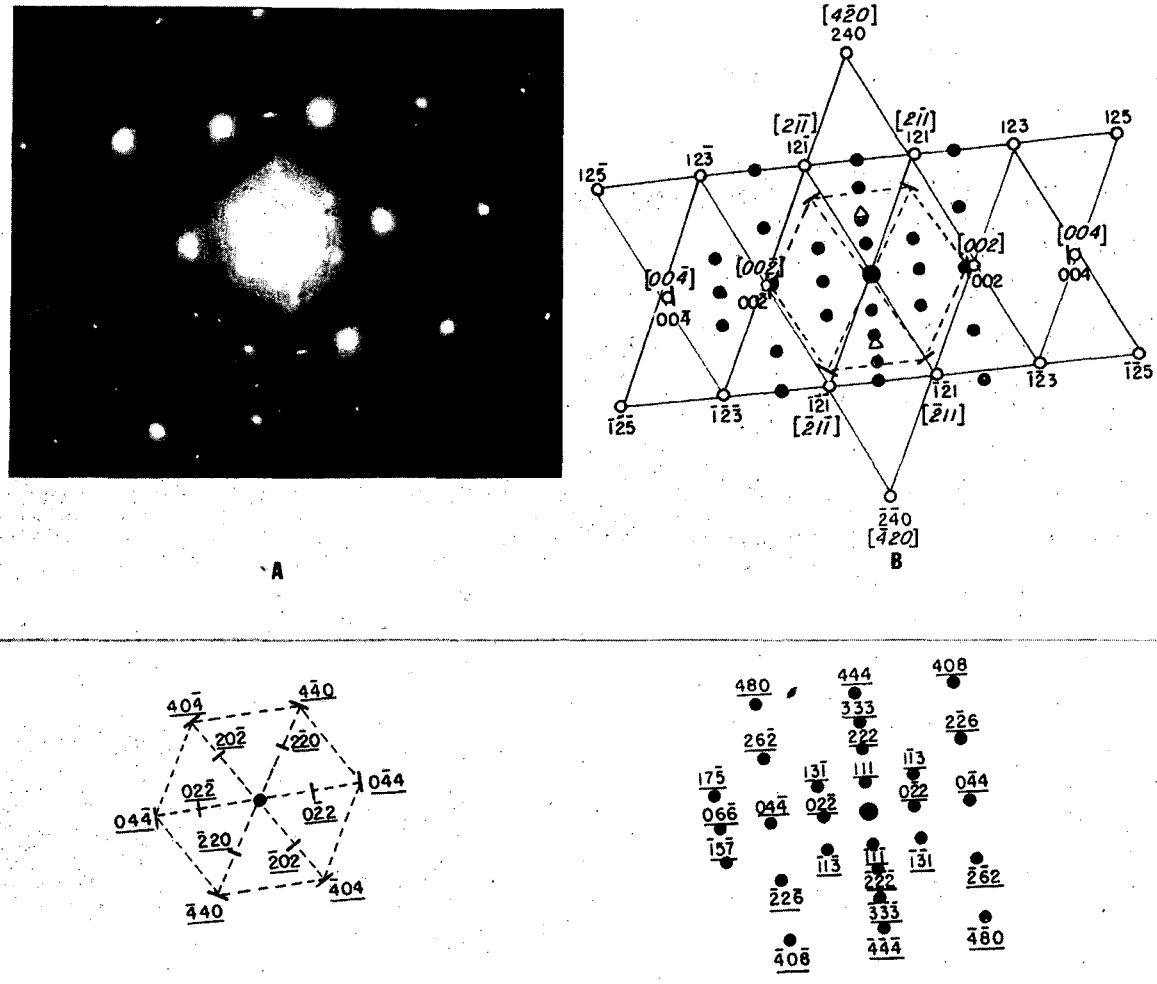

Fig. 6. (a) Diffraction pattern taken from an area showing the $[\bar{2}10]_{\alpha}$ zone (or $[120]_{\alpha}$ zone) and two variants of the oxide ($[\underline{\bar{2}11}]_{oxide}$ and $[\underline{111}]_{oxide}$ zones). (b) Index of the diffraction pattern (o - $[\bar{2}10]_{\alpha}$ zone or $[120]_{\alpha}$ zone, ● - $[\underline{\bar{2}11}]_{oxide}$ zone, / - $[\underline{111}]_{oxide}$ zone, Δ - Relrod effect from next layer of the reciprocal lattice of the b.c.c. matrix). (c) Index of the $[\underline{\bar{2}11}]_{oxide}$ zone corresponding to $[\bar{2}10]_{\alpha}$ zone. (d) Index of the $[\underline{111}]_{oxide}$ zone corresponding to $[120]_{\alpha}$ zone.

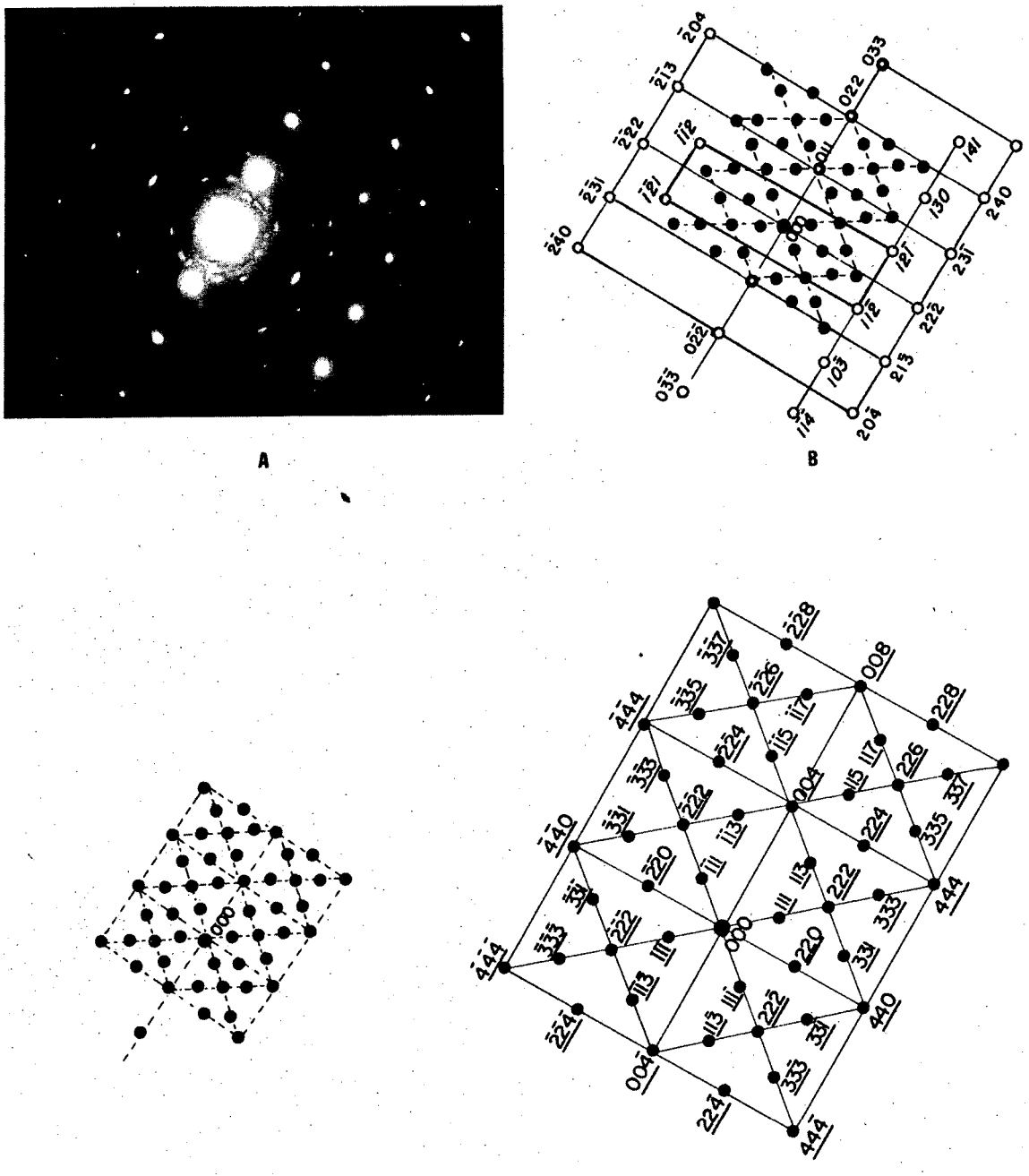

Fig. 7. (a) Diffraction pattern taken from an area with a matrix zone orientation between $[2\bar{1}1]_\alpha$ and $[3\bar{7}1]_\alpha$ showing the $[1\underline{\bar{1}0}]_{oxide}$ zone. (b) Index of the diffraction pattern (o - $[2\bar{1}1]_\alpha$ zone or $[3\bar{7}1]_\alpha$ zone, ● - $[1\underline{\bar{1}0}]_{oxide}$ zone. (c) The $[1\underline{\bar{1}0}]_{oxide}$ zone. (d) Enlargement and index of the $[110]_{oxide}$ zone.

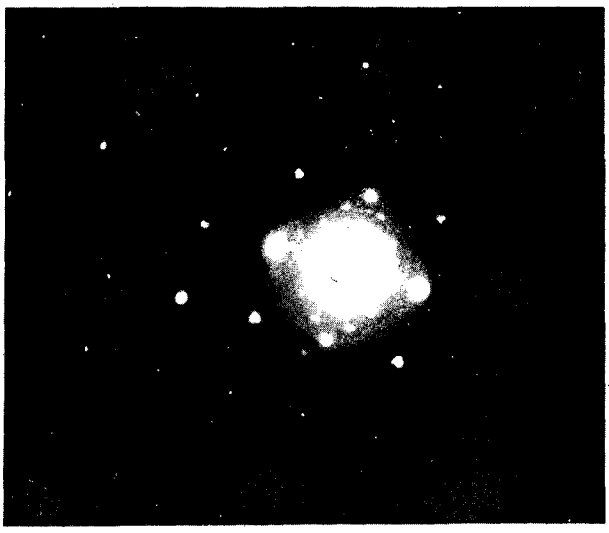

A

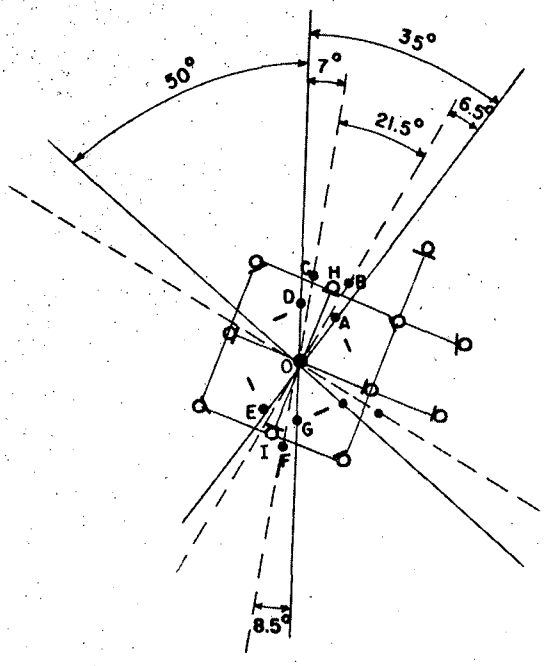

B

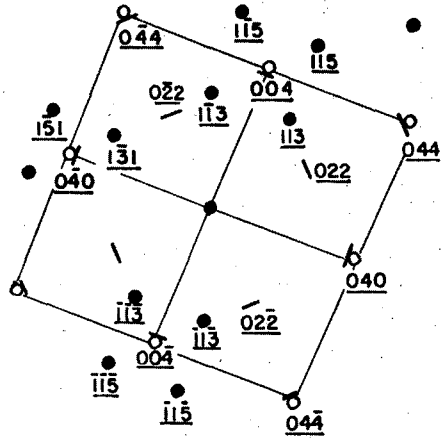

C

XBB 7512-9244

Fig. 8. (a) Electron diffraction pattern taken from an area which shows the $[100]_{\alpha}$ and $[\underline{100}]_{oxide}$ zone with relrod effect.
(b) The angular relationship between the diffraction spots.
(c) Index of the diffraction pattern.

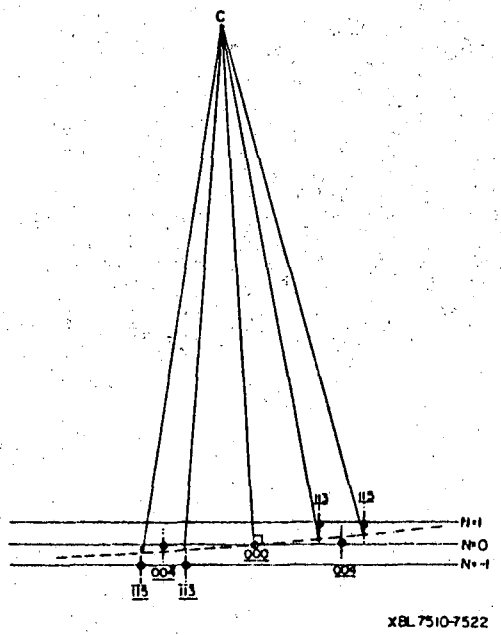

Fig. 9. The diffraction condition for the occurrence of the relrod effect due to a small misorientation of the exact $[\underline{100}]_{oxide}$ zone.

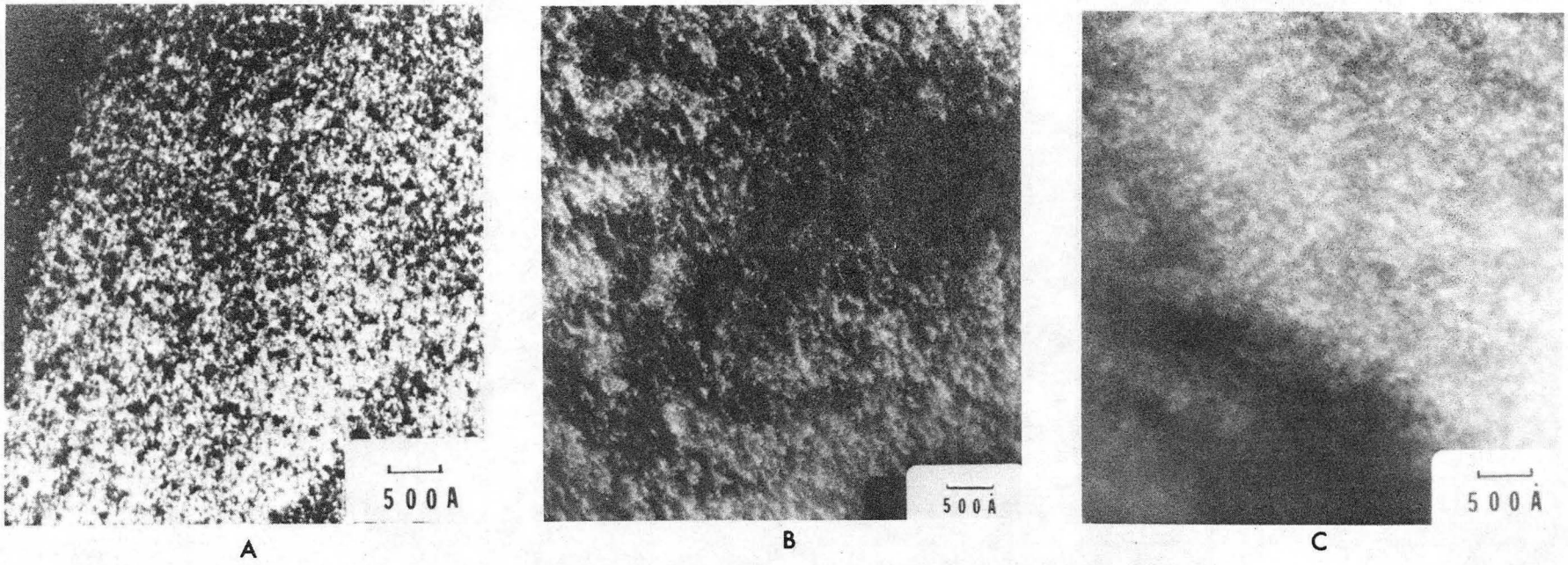

XBB 763-2341

Fig. 10. Morphology of the thin oxide layer. (a) The dark field micrograph taken from the $(\underline{113})_{oxide}$ diffraction with sample oriented in the $[113]_{\alpha}$ direction. (b) Dark field micrograph taken from the $(\underline{404})_{oxide}$ diffraction spot with sample oriented in the $[110]_{\alpha}$ zone. (c) Dark field micrograph taken from the $(\underline{1\bar{1}3})_{oxide}$ diffraction spot with sample oriented in the $[100]_{\alpha}$ orientation.

TECHNICAL INFORMATION DIVISION
LAWRENCE BERKELEY LABORATORY
UNIVERSITY OF CALIFORNIA
BERKELEY, CALIFORNIA 94720